ECS | The Electrochemical Society
Advancing solid state & electrochemical science & technology

Ionic Liquid-Packed Microfluidic Device with Non-Planar Microelectrode as a Miniaturized Electrochemical Gas Sensor

To cite this article: Sreerag Kaaliveetil *et al* 2023 *J. Electrochem. Soc.* **170** 087508

View the article online for updates and enhancements.

CrossMark

Ionic Liquid-Packed Microfluidic Device with Non-Planar Microelectrode as a Miniaturized Electrochemical Gas Sensor

Sreerag Kaaliveetil,[1] Yun-Yang Lee,[2] Zhenglong Li,[1] Yu-Hsuan Cheng,[1] Niranjan Haridas Menon,[1] Saudagar Dongare,[2] Burcu Gurkan,[2] and Sagnik Basuray[1,3,z]

[1]Department of Chemical and Materials Engineering, New Jersey Institute of Technology, Newark, New Jersey 07102, United States of America
[2]Department of Chemical and Biomolecular Engineering, Case Western Reserve University, Cleveland, Ohio 44106, United States of America
[3]Department of Biomedical Engineering, New Jersey Institute of Technology, Newark, New Jersey 07102, United States of America

Integrating transducer/sensing materials into microfluidic platforms has enhanced gas sensors' sensitivity, selectivity, and response time while facilitating miniaturization. In this manuscript, microfluidics has been integrated with non-planar microelectrode array and functionalized ionic liquids (ILs) to develop a novel miniaturized electrochemical gas sensor architecture. The sensor employs the IL 1-ethyl-3-methylimidazolium 2-cyanopyrolide ([EMIM][2-CNpyr]) as the electrolyte and capture molecule for detecting carbon dioxide (CO_2). The three-layer architecture of the sensor consists of a microchannel with the IL sandwiched between glass slides containing microelectrode arrays, forming a non-planar structure. This design facilitates electric field penetration through the IL, capturing CO_2 binding perturbations throughout the channel volume to enhance sensitivity. CO_2 binding with [EMIM][2-CNpyr] generates carboxylate ([EMIM]$^+$-CO$_2^-$), carbamate ([2-CNpyr]-CO$_2^-$), and pyrrole-2-carbonitrile (2-CNpyrH) species, significantly decreasing the conductivity. The viscosity is also increased, leading to a further decrease in conductivity. These cumulative effects increase charge transfer resistance in the impedance spectrum, allowing a linear calibration curve obtained using Langmuir Isotherm. The sensitivity and reproducibility in CO_2 detection are demonstrated by two electrode configurations using the calibration curve. The developed sensor offers a versatile platform for future applications.
© 2023 The Electrochemical Society ("ECS"). Published on behalf of ECS by IOP Publishing Limited. [DOI: 10.1149/1945-7111/aced6e]

Gas sensors are mainly used in applications like monitoring indoor air quality, detecting explosive and toxic gases, and breath analysis. Integrating gas sensors with portable systems can increase their deployment in multiple areas like environmental monitoring,[1] indoor air quality monitoring,[2] the medical sector,[3] agricultural industries,[4] and the transportation sector. Thus the present research focuses on developing miniaturized gas sensors[5] without compromising critical parameters like selectivity, sensitivity, and response time. Microfluidics allows for the development of miniaturized gas sensors due to the minimal use and consumption of reagents with improved reaction speed, mass transfer, and heat transfer.[6]

Different detection techniques have been incorporated with microfluidics, which includes metal oxide semiconductor (MOS), electrochemical, optical techniques like fluorescence, and surface-enhanced Raman spectroscopy (SERS), to develop portable sensors. Among these, the most widely researched is MOS sensors due to their low cost and high sensitivity. However, the main problem with MOS sensors is their poor selectivity. This is because, in general, the MOS does not have an affinity to any particular gas. For instance, the interaction of an n-type MOS sensor with any reducing gases (like ammonia, carbon monoxide, hydrogen, or volatile organic compounds (VOCs)) decreases the resistance of the MOS sensor. In contrast, interacting with oxidizing gases increases the resistance.[7] Even though microfluidics is incorporated with MOS sensors to introduce some level of selectivity,[8–12] it is still challenging to selectively detect gases from a complex mixture. On the other hand, SERS-based sensors show high sensitivity (in ppb levels[13–16]); however, their high cost, complexity in fabrication, and lack of portability impede the deployment of SERS-based miniaturized gas sensors.

Electrochemical gas sensors are the most promising solution for miniaturized gas sensors. Electrochemical gas sensors provide high sensitivity at a low cost.[17] Moreover, they can be developed in a portable form factor by miniaturizing the electrodes and using a

portable potentiostat with very low power consumption.[18] Various materials have been employed as the transducer component in electrochemical sensors. These primarily encompass diverse classes of nanomaterials such as metal-organic frameworks (MOFs),[19] carbon-based nanomaterials,[20,21] and two-dimensional layered nanomaterials like MXenes,[22] carbon nitrides,[23] among others. In certain instances, the supporting electrolyte serves as the transducer element itself. This generally occurs when room-temperature ionic liquid (RTILs) is utilized as the electrolyte.[24]

The major drawbacks of electrochemical gas sensors originate from using conventional electrolytes. Conventional aqueous electrolytes like H_2SO_4/H_2O, which are widely used in commercial gas sensors, are prone to evaporative losses, which decrease the lifetime of the sensor.[17] In addition, the narrow electrochemical window of these electrolytes prevents these sensors from detecting certain gases. Due to these limitations, researchers have developed electrochemical gas sensors that employ RTILs as electrolytes.[24–27] RTILs are salts with a melting point lower than room temperature. RTILs have several desired characteristics, like low volatility, wide electrochemical window, intrinsic conductivity, and high chemical stability, making them an ideal candidate for electrolytes in electrochemical gas sensors.[28] Moreover, they have high solubility for a broad range of gases and VOCs, making them both a solvent and an electrolyte in the electrochemical gas sensors.[29]

The use of microfluidics for developing electrochemical sensors to analyze liquid samples has been widely adopted. It is used in detecting biological analytes like DNA and proteins,[30] heavy metals like Fe^{3+} and Hg^{2+},[31] and contaminants like per- and poly-fluoroalkyl substances.[32] However, its application in developing chemical gas sensors must be more utilized. In this work, microfluidics is combined with microelectrode technology to develop a miniaturized electrochemical gas sensor that uses an RTIL functionalized for selective capture of CO_2. RTILs can be tuned for specific affinity towards other gases and target analytes;[33–36] CO_2 is used as a model gas to show the proof of concept of the electrochemical sensor. The developed microfluidic electrochemical sensor has a non-planar microelectrode configuration, which has performed better

[z]E-mail: sbasuray@njit.edu

in previous studies than a planar architecture.[31] Using non-planar architecture allows the penetration of the electric field through the microchannel, thus allowing us to register any perturbation caused by the binding of CO_2 to the RTIL from the entire volume of the channel, which is filled with RTIL. 1-Ethyl-3-methylimidazolium 2-cyanopyrolide ([EMIM][2-CNpyr]) is used as the functionalized RTIL, as it has been demonstrated previously[37] to have high CO_2 solubility at low CO_2 partial pressures. Accordingly, the absorption of CO_2 by [EMIM][2-CNpyr] results in the formation of carboxylate ([EMIM]$^+$-CO_2^-), carbamate ([2-CNpyr]-CO_2^-), and pyrrole-2-carbonitrile (2-CNpyrH) species under anhydrous condition. When moisture is present, water is also absorbed by the RTIL, and the absorbed water reacts with CO_2 through the protonation of [2-CNpyr]$^-$ forming the neutral pyrrole-2-carbonitrile (2-CNpyrH) along with bicarbonate. As the CO_2 absorption products under both anhydrous and moist conditions engage in hydrogen bonding, both the viscosity and density increase. As a result, the ionic conductivity decreases, as reported previously for functionalized RTILs;[38] similar behavior is observed here. These changes occurring in the RTIL due to the chemical absorption of CO_2 are captured using electrochemical impedance spectroscopy (EIS) using two different electrode configurations, namely near electrode configuration (NEC) and far electrode configuration (FEC). In NEC, the distance between electrodes is equal to the thickness of the microchannel (140 μm), and the electric fields are restricted to the vertical direction. In FEC, the distance between electrodes is much larger, around 4 mm, and the electric field has vertical and horizontal components. The sensitivity and reproducibility of both electrode configurations were analyzed, and they showed nearly equal sensitivity. However, the FEC showed much better reproducibility. A very high linear range for the CO_2 feed, from 410 to 50000 ppm, was obtained from the calibration curve of both electrode configurations.

Experimental

Reagents and instruments.—Standard glass slides were obtained from globe scientific to fabricate the top and bottom glass slides containing the microelectrode arrays. A double-sided polypropylene tape with a thickness of 142 μm is used to fabricate the microchannel. Electrochemical impedance measurements (EIS) were obtained using an Agilent 4294 A impedance analyzer from Keysight. Cyclic voltammetry (CV) measurements were obtained using Gamry Reference 600+ potentiostat. The microelectrode arrays′ top and bottom glass slides are fabricated in the Nanofabrication facility at CUNY Advanced Science Research Center.

1-Ethyl-3-methyl-imidazolium chloride ([EMIM][Cl], 99%) was purchased from TCI America; methanol (HPLC grade), pyrrole 2-carbonitrile (99%), and amberlite IRN-87 anion-exchange resin (AER) was purchased from Alfa Aesar. Obtained AER was washed with methanol multiple times and vacuum-dried overnight at room temperature. Nitrogen (N_2, Ultra High Purity) and carbon dioxide (CO_2, Bone Dry) were obtained from Airgas.

Synthesis of 1-ethyl-3-methylimidazolium 2-cyanopyrolide and sample preparation.—[EMIM][2-CNpyr] was synthesized using the previously reported procedure[37] employing an anion-exchange reaction followed by acid-base neutralization. Briefly, [EMIM][Cl] was first converted to [EMIM][OH] in methanol using AER in a column. Pyrrole-2-carbonitrile was then added to the obtained solution of [EMIM][OH] for the acid-base reaction, which then produced [EMIM][2-CNpyr] in an aqueous methanol solution. Excess methanol was removed by rotary evaporation at 70 °C for an hour, and residual water was removed under a high vacuum at 80 °C for two days. NMR characterization was performed to confirm the synthesized RTIL (See Fig. S1), similar to previous reports.[37,39]

Samples for EIS measurements were prepared by exposing [EMIM][2-CNpyr] to CO_2/N_2 gas mixtures for two hours at 22 °C. The concentration of CO_2 in the feed gas (0 to 50000 ppm) was

varied by mass flow controllers on N_2 and CO_2 feed gas lines (Brooks 5850I) using LabVIEW. The gas analyzer (SBA-5, PPSystems Inc.) was used to monitor the CO_2 concentrations in the feed gas to confirm the supplied partial pressure of CO_2 to the RTIL. Figure S2 shows the ^{13}C NMR of RTIL before and after absorption of CO_2 under 1 bar of CO_2 and 22 °C with 0 and 40% relative humidity, demonstrating the carboxylate, carbamate, and bicarbonate peaks. The RTILs exposed to CO_2 were directly incorporated into the microfluidic platform to perform EIS measurements (as shown in Fig. S3) as detailed in assembling the microfluidic platform section.

Conductivity and viscosity measurement.—A commercial conductivity cell formed from borosilicate glass, with two platinum black electrodes (MMA 500 from Biologic INC), was used to measure ionic conductivities of the RTIL with various CO_2 saturation levels. In addition, viscosities for the same samples were measured with a microchannel viscometer (Micro-VISC, Rheosense). All of the measurements were performed at 22 ± 1 °C.

Fabrication of platinum microelectrode array.—Microelectrodes are fabricated using standard lithographic techniques. First, the glass slides are cleaned using piranha solution (Sulphuric acid and hydrogen peroxide mixed in a 3:1 ratio). The glass slide is then dehydrated in the hot plate at 130 °C for 15 min. Next, hexamethyldisilazane (HMDS) is spin coated to make the glass slide hydrophobic, after which AZ1512 positive photoresist is spin-coated. The pattern is then created on the glass slide by using a mask (with the electrode pattern) and exposing the glass substrate to UV light (of intensity 350 mJ cm^{-2}) with the help of an EVG620 mask aligner. The glass slide is then placed in a developer (AZ300 MIF) for 30 s and washed with DI water. An electron beam evaporation system, Orion-8E, AJA International, is used for the deposition. Next, a 10 nm chromium layer is deposited to ensure the adhesion of the deposited 100 nm platinum (Pt) layer. After the deposition, the glass slides are placed in the acetone solution for the lift-off.

Fabrication of microchannel.—Polypropylene double-sided adhesive tape is used as the substrate to fabricate the microchannels. A Cricut machine is used to cut microchannels on the polypropylene tape with a length of 65 mm, a width of 500 μm, and a thickness of 140 μm.

Assembling the microfluidic platform.—The device consists of three parts (as shown in Fig. 1) (i) a top glass slide containing a Pt microelectrode array, (ii) polypropylene double-side tape containing a microchannel, and (iii) a bottom glass slide containing microelectrode arrays. First, two holes (inlet and outlet) are drilled on the top glass slide using a 1 mm drill bit. Next, the double-sided tape containing the microchannel is pasted on the top glass slide so that the holes (inlet and outlet) and the microelectrodes lie inside the microchannel. The bottom glass slide is then affixed onto the adhesive tape so that the microelectrode (in the bottom) is aligned with the top glass slide interdigitated. Flow ports are then fixed on the top glass slide, and the entire device is sealed using epoxy. After assembling the device, the ionic liquid is injected using a 3 ml syringe into the microchannel through the inlet port under the microscope till the ionic liquid is seen on the opposite port. This ensures that the whole channel is filled with only ionic liquid and no air.

Electrochemical measurements.—The impedance spectrum of the microfluidic platform is recorded using Agilent 4294 A. The impedance spectrum of the microfluidic platform (containing the RTIL, [EMIM][2-CNpyr], exposed to CO_2) is recorded in a frequency range of 1 kHz to 100 MHz with an oscillator (OSC) level of 500 mV. It is important to note that the DC bias function is
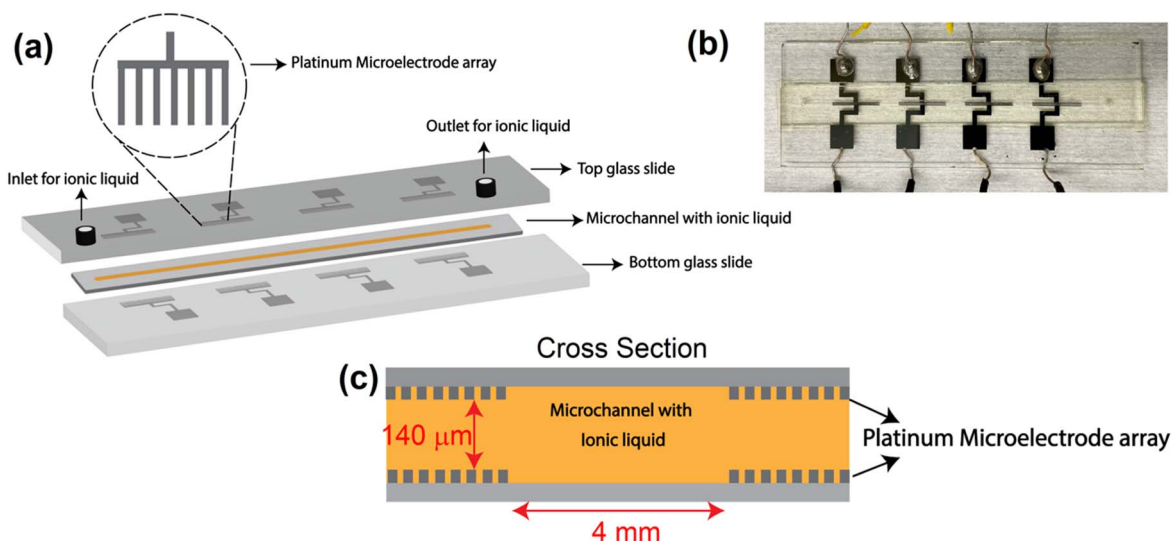
Figure 1. (a) Schematic of the microfluidic device with three layers. The top layer contains platinum microelectrode arrays in a glass substrate. The middle layer is polyethylene tape with a microchannel that contains ionic liquid. The bottom layer contains platinum microelectrode array in a glass substrate. (b) Image of the assembled device. (c) Cross-sectional view of a part of the device.
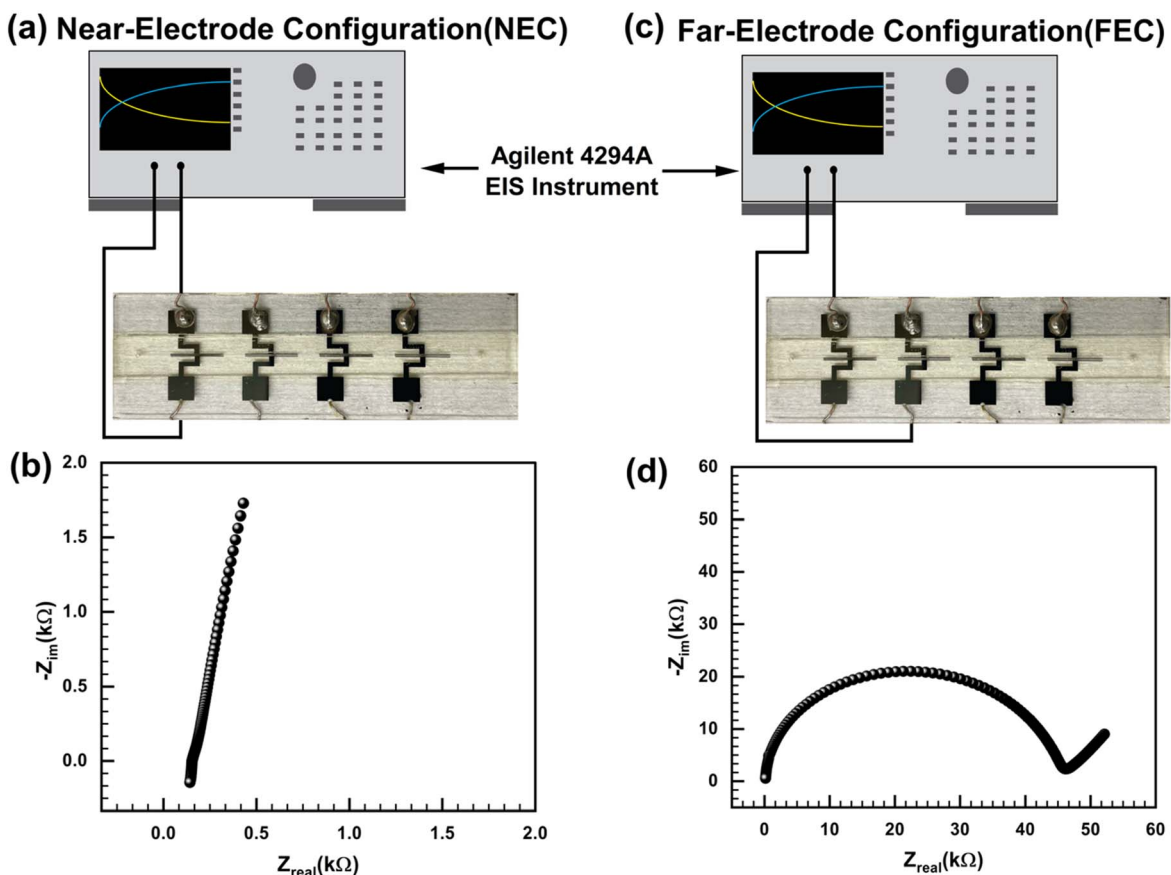

Figure 2. (a) Schematic of NEC. In NEC, the separation between the two electrodes is 140 μm. (b) Characteristic impedance spectrum produced by NEC. (c) Schematic showing FEC configuration. In FEC the separation between the electrodes is approximately 4 mm. (d) Characteristic impedance spectrum produced by FEC.

turned off while taking the measurement. CV experiments were done using Gamry Reference 600+ potentiostat. All the CV experiments were performed between a potential range of −0.7 to +0.7 V using a two-electrode setup where the working and working sense are connected to the platinum working electrode in the chip. In contrast, the reference and the counter electrode were connected to the platinum counter electrode in the chip. As a result, the impedance and CV of two different electrode configurations are recorded (i) near-electrode configuration (NEC) and (ii) far-electrode configuration (FEC). The two electrode configurations and their characteristic impedance spectrum are shown in Fig. 2, while the CV is shown in Fig. 6.
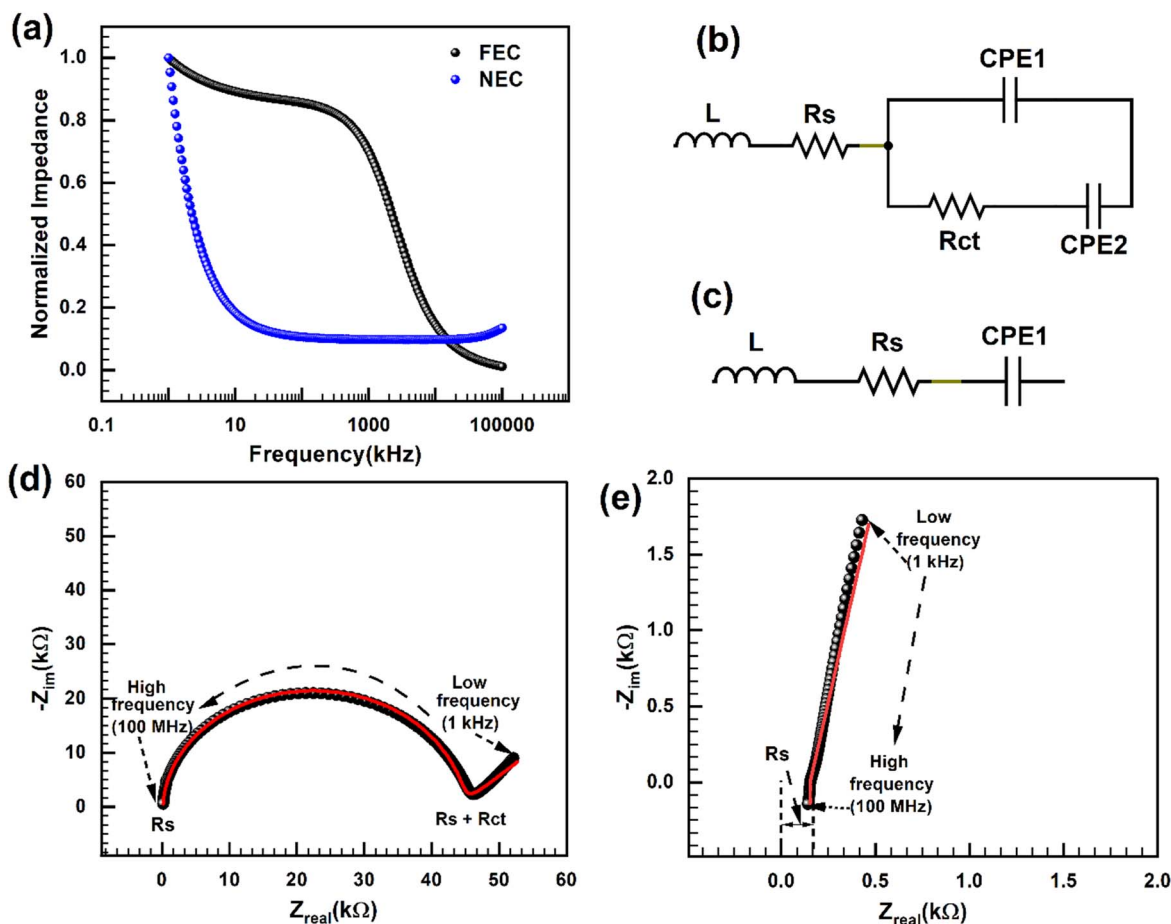
Figure 3. (a) Bode plot of FEC and NEC configuration. (b) Proposed equivalent circuit model for FEC configuration and (c) NEC configuration. (d) Nyquist plot showing the fitting curve (red line) of FEC configuration and (e) NEC configurations.

Results and Discussion

Electrochemical impedance characterization of the microfluidic platform.—The microfluidic platform consists of four electrode pairs which can be used in two different electrode configurations, i.e., near electrode configuration (NEC) and far electrode configuration (FEC). These two electrode configurations and their corresponding impedance spectrum (Nyquist plot) are shown in Fig. 2. These impedance spectrums are recorded using [EMIM][2-CNpyr] as the electrolyte filled in the microchannel. In the NEC, the distance between the electrodes is 142 μm (thickness of the microchannel), while in the case of FEC, the distance between the electrodes is approximately 4 mm. Furthermore, in the NEC, the electric field is restricted in the vertical direction. In contrast, the electric field in the FEC has both vertical and horizontal components.

Due to these reasons, each electrode configuration produces characteristic impedance signatures, as shown in Fig. 1. The Nyquist and the Bode plot (Fig. 3a) for FEC produces a characteristic spectrum corresponding to a Randles circuit (Fig. 3b). At the lower frequencies, the diffusion process dominates, represented by the constant phase element (CPE2) in the Randles circuit. At mid to higher frequencies, the impedance is predominantly due to two parallel processes, i.e., double-layer capacitance and charge transfer resistance represented by a constant phase element (CPE1) and resistor (Rct). The solution resistance is represented by a series resistor (Rs). The result of fitting the impedance spectrum of FEC with the Randles circuit is shown in Fig. 3d. The values of circuit components obtained after fitting are shown in Table I. In the case of NEC, the diffusion process dominates the entire frequency range, as evident from the Nyquist plot. Also, analyzing the Bode plot, which resembles the impedance spectrum of resistor and capacitor

connected in series, it is clear that NEC can be fitted with the circuit shown in Fig. 3c. The result of this fitting is shown in Fig. 3e. A mismatch exists between the experimental value and the fitted curve at lower frequencies or higher impedance. In this study, we are interested in the impedance at higher frequencies for NEC. Hence the deviation (between the experimental and fitted curve) at higher impedance values does not interfere with the analysis or impact conclusions. To further understand the impedance behavior of the microfluidic platform, two parameters were varied, namely, (1) the thickness of the microchannel and (2) the distance between two electrodes in the FEC. The Nyquist plot of NEC and FEC configuration at different microchannel thicknesses (140, 280, and 420 μm) is shown in Figs. 4a and 4b. In the case of NEC, the series resistance increases as the thickness of the microchannel increases due to the increase in distance between the electrodes. While in the case of FEC, the size of the semicircle (the charge transfer resistance) decreases with increased channel length. To understand this, it is important to note that FEC has a horizontal component of the electric field and hence a horizontal component of ionic flux. As the thickness of the microchannel increases, the cross-sectional area of the microchannel increases, which increases the ionic current and decreases the impedance.

The second parameter varied is the distance between the electrodes in FEC by keeping the microchannel thickness constant. It is important to mention that the electrochemical cell consists of 4 electrode pairs. Therefore, the distance between the electrodes in the FEC can be varied by choosing different electrode pairs, as shown in Fig. 4c. Figure 4d shows that increasing the distance between electrodes in FEC increases the charge transfer resistance. In addition, increasing the distance between electrodes increases the

Table I. Values of circuit components for FEC and NEC obtained after fitting the equivalent circuit models shown in Figs. 3b and 3c to the corresponding impedance spectrums shown in Figs. 3d and 3e.

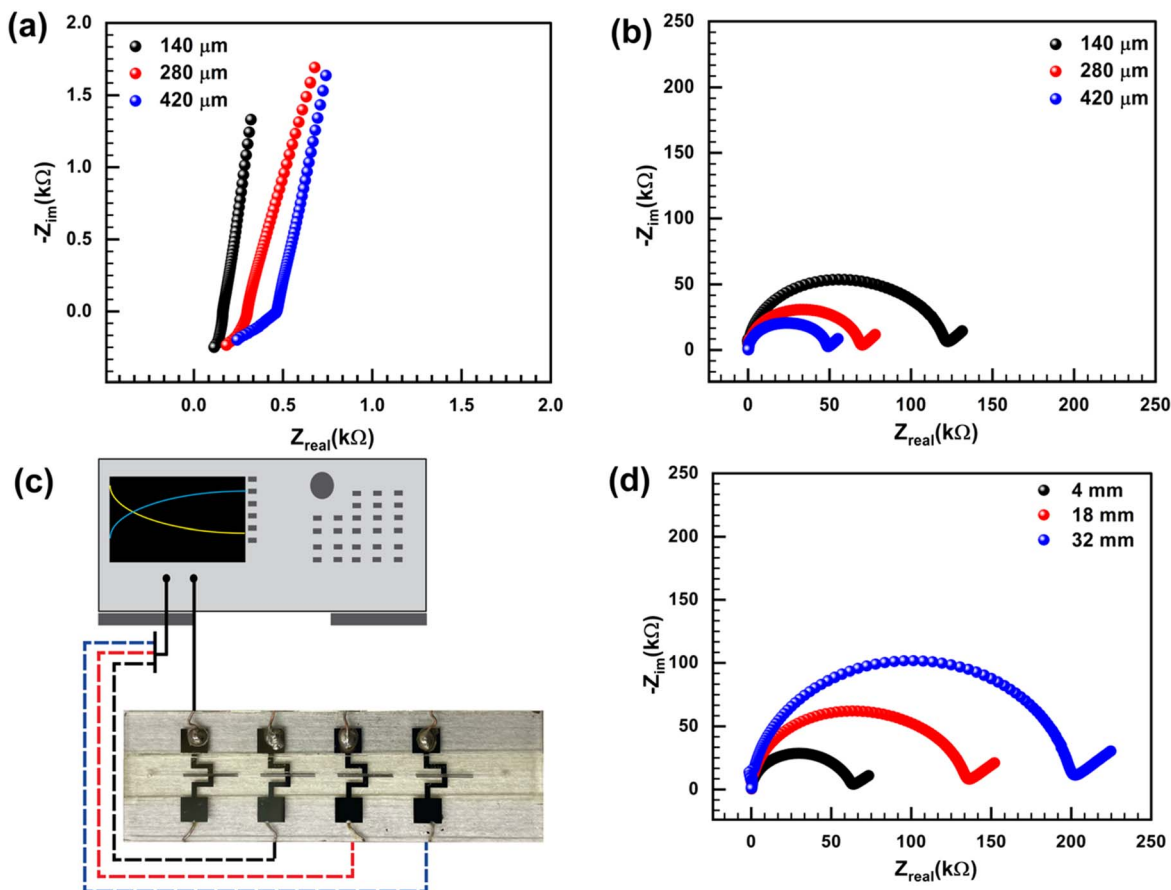| Config.	L (H)	Rs (Ω)	CPE 1		Rct (Ω)	CPE 2		Weighted χ^2
			Q1	n1		Q2	n2	
FEC	$4.23 \times 10^{-7} \pm 5.10 \times 10^{-9}$	127 ± 2.25	$2.95 \times 10^{-12} \pm 3.47 \times 10^{-14}$	$9.79 \times 10^{-1} \pm 6.66 \times 10^{-4}$	$4.41 \times 10^4 \pm 6.22 \times 10^1$	$1.13 \times 10^{-6} \pm 6.47 \times 10^{-8}$	$4.93 \times 10^{-1} \pm 6.37 \times 10^{-3}$	5.47×10^{-5}
NEC	$2.43 \times 10^{-7} \pm 1.12 \times 10^{-9}$	153 ± 0.17	$2.53 \times 10^{-7} \pm 2.83 \times 10^{-9}$	$8.85 \times 10^{-1} \pm 1.08 \times 10^{-3}$	—	—	—	1.66×10^{-4}

Figure 4. Nyquist plot of (a) NEC and (b) FEC with different microchannel thickness (140, 280 and 420 μm). (c) Schematic showing the selection of different pairs of electrodes to increase the distance between the electrodes in FEC configuration. (d) Nyquist plot of FEC with different distance between the electrodes (4, 10 and 32 mm).

ohmic drop, leading to a concomitant decrease in the current produced during any charge transfer process.[31]

Detection of CO_2 in the ionic liquid.—The impedance spectrums of a microfluidic platform with the ionic liquid, [EMIM][2-CNpyr], exposed to a CO_2/N_2 gas mixture containing different concentrations of CO_2 (in the range of 0 to 50000 ppm) are shown in Fig. 5. It should be noted that the values of CO_2 concentration shown in these graphs are the CO_2 concentration present in the gas feed and not the concentration of CO_2 absorbed by the IL. In the NEC, there is a shift in the impedance spectrum in the Nyquist plot along the *x*-axis as the CO_2 concentration in [EMIM][2-CNpyr] increases (Fig. 5a). This change is also reflected in the Bode plot at a higher frequency range (Fig. S4a). By fitting the impedance spectrum of NEC with the equivalent circuit shown in Fig. 3c, it is observed that the x-offset corresponds to the change in the series resistance (values of fitting parameters are shown in Table SI, and the fitted spectrum is shown in Fig. S5a). Hence the value of the series resistance is used to create the calibration curve (the calibration curve created using parameters from the equivalent circuit will be called a parameter-based calibration curve) shown in Fig. S6a, which shows exponential relation. Such a relation is expected since the CO_2 absorption isotherm of [EMIM][2-CNpyr] follows the Langmuir model, as shown by Lee et al.[37] A linear relationship can be obtained using a semi-logarithmic scale, as shown in Fig. 5c. For the impedance spectra of FEC, the diameter of the semicircle increases, i.e., the charge transfer resistance increases as the concentration of CO_2 in the IL increases (Fig. 5b). This change is reflected in the Bode plot at lower frequency regions (Fig. S4b). The charge transfer resistance, obtained by fitting the Randles circuit (values of fitting parameters shown in Table SII and the fitted spectrum is shown in Fig. S5b) to

the individual impedance spectra in FEC, is used to create a parameter-based calibration curve, as shown in Fig. 5d. Like the NEC, the parameter-based calibration curve for FEC shows a linear range when plotted in a logarithmic scale from 410 to 50000 ppm.

The cyclic voltammetry (CV) curves for both electrode configurations are shown in Fig. 6. In both configurations, the peak value of the current gradually decreases as the concentration of CO_2 in feed gas and, therefore, in the IL increases. It is hypothesized that the changes in the impedance spectrum and CV curve (as the concentration of CO_2 increases) are due to the modifications of ions in IL due to the chemical absorption of CO_2. [EMIM][2-CNpyr] chemically absorb CO_2, which modifies both the anion and cations in the IL.[39] As reported previously, there are two reactions pathways: (i) complexation of CO_2 with [2-CNpyr]$^-$ forming carbamate ($-$N–COO) and (ii) complexation of CO_2 with [EMIM]$^+$ generating carboxylate ($-$C–COO) species under anhydrous conditions. The carboxylate formation is possible by deprotonating [EMIM]$^+$ to carbene, which binds with CO_2. The hydrogen transfer from the cation to the anion yields the carbene while neutralizing the anion to pyrrole-2-carbonitrile. Additionally, bicarbonate forms under moist conditions since the absorbed CO_2 and water further react in the IL phase.[37] These compositional changes influenced the measured viscosity and ionic conductivity as shown in Fig. S7: the viscosity increases and the ionic conductivity decreases with increasing CO_2 saturation in [EMIM][2-CNpyr]. These trends are consistent with the increasing Rct in EIS and the decreasing peak currents in the CVs, where the higher CO_2 concentration in the feed gas generates a more viscous liquid, thereby hindering the diffusion of ions toward the electrode surface and increasing the charge transfer resistance. We hypothesize that viscosity and ionic conductivity changes contribute to the overall change in Rct. Though it is difficult to segregate the
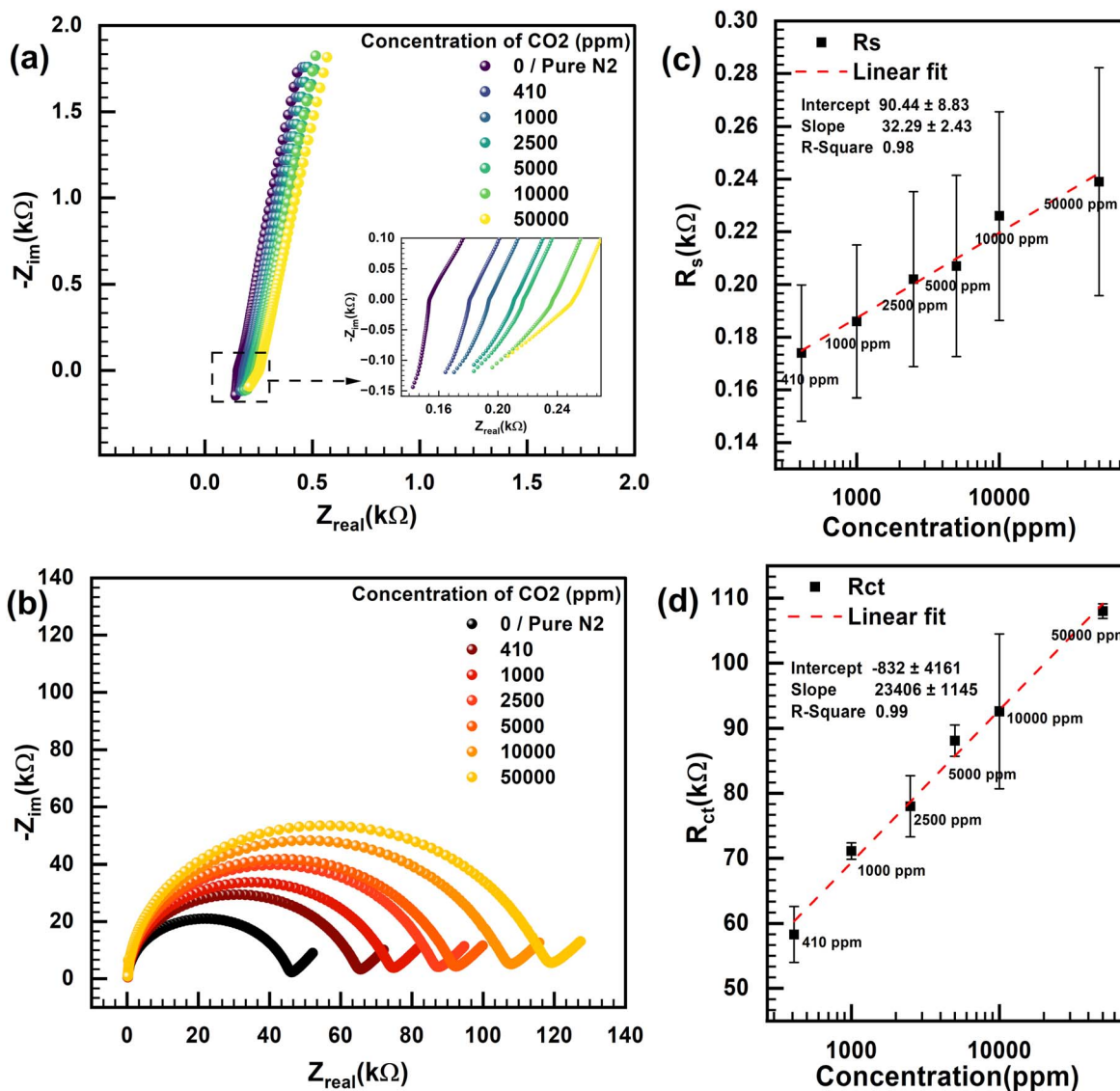
Figure 5. Impedance spectrum (Nyquist plot) of (a) NEC and (b) FEC with ionic liquid containing different concentration of CO_2. Calibration curve for (c) NEC and (d) FEC. Calibration curve is obtained by plotting the Rs (for NEC) and Rct (FEC) values obtained from fitting the equivalent circuit model (shown in Figs. 3b and 3c) for different concentration of CO_2.
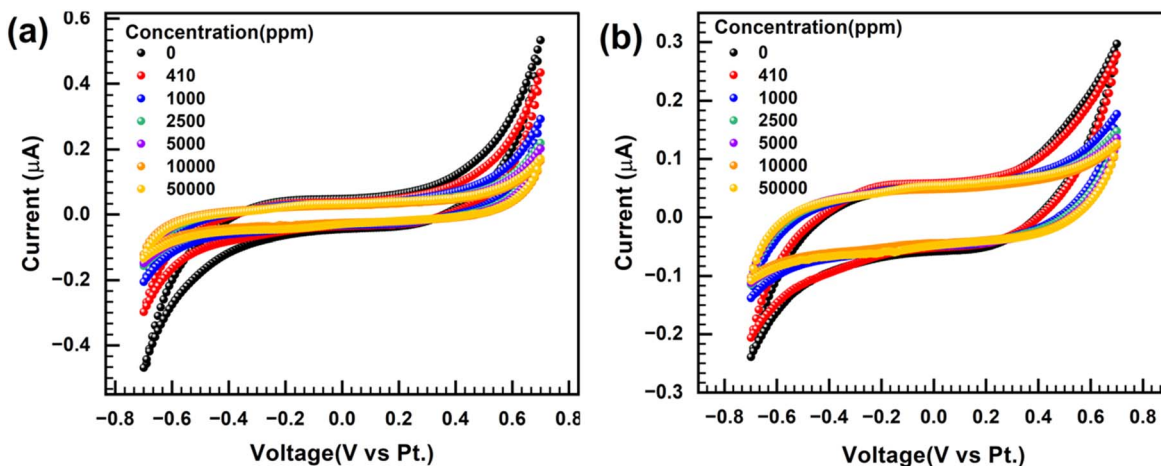

Figure 6. Cyclic voltammetry curves of (a) NEC and (b) FEC with ionic liquid exposed with different concentrations of CO_2.
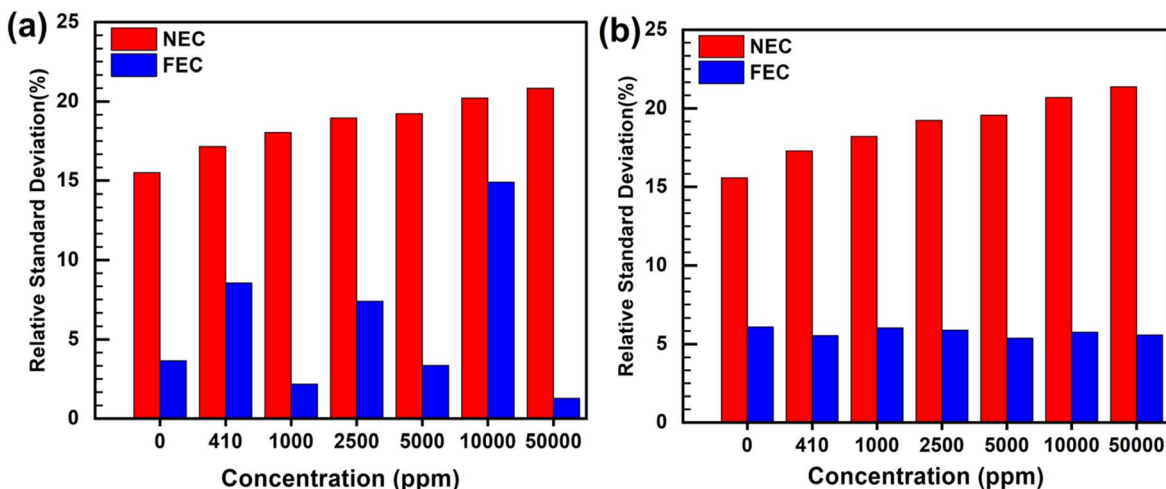
Figure 7. Relative standard deviation of NEC and FEC from (a) parameter-based calibration curve and (b) fixed-frequency based calibration curve. The fixed frequency-based calibration curve is used to eliminate the contribution of error from fitting.

individual effect of each phenomenon on the overall Rct, these changes are cumulative. They thus allow the creation of a linear calibration curve that maps the change in the Rct with a change in CO_2 concentration using a Langmuir Isotherm.

The limit of detection (LOD) is determined using the equation below[40] to compare the sensitivity of both electrode configurations.

$$LOD = \frac{3*S_a}{b}$$

Here Sa is the standard deviation of the y-intercept, and b is the slope the of the calibration curve. The LOD for NEC and FEC is very similar and is found to be 0.82ppm and 0.53ppm. From this, it can be concluded that the electrode configuration will not significantly change the sensor′s sensitivity. However, to determine which system is better, multiple experiments were conducted to examine the reproducibility of both systems by measuring the relative standard deviation (RSD).[41] The RSD of every point in the NEC and FEC calibration curves is shown in Fig. 7a. From the graph, it is very clear that the RSD for FEC is smaller for all the concentrations. In this case, the RSD is not only from the experiments but also from the fitting. Therefore, a fixed frequency calibration curve is created, as shown in Fig. S8, to eliminate the error from fitting. In the fixed frequency calibration curve, an impedance value at a specific frequency is chosen that closely corresponds to the impedance of Rs and Rct in NEC and FEC configuration, respectively. The RSD obtained from this calibration curve is shown in Fig. 7b. Again, FEC ′s RSD is smaller than NEC′s for all concentrations. These results suggest that FEC shows better reproducibility compared to NEC. This is because in NEC since the electrodes are very close to each other (142 μm apart), even a slight change in alignment between the two electrodes or slight damage in the electrode fingers might result in significant impedance changes. Furthermore, since the devices are manually assembled, misalignments will inevitably occur. Performing the assembling through a robotic system could reduce the misalignments between the electrode pairs, thereby reducing the RSD. However, in FEC, since the electrodes are already placed significantly away from each other (4 mm apart), changes in the electrode alignment might not contribute to the significant changes in the impedance spectrum. Hence, when manually assembling the device, FEC will give better reproducible results.

Conclusions

This work combines microfluidics, ILs, and non-planar microelectrode array technology to develop a novel electrochemical gas sensor to detect CO_2. The platform comprises a microfluidic channel

sandwiched between two glass slides containing microelectrode arrays. An ionic liquid, [EMIM][2-CNpyr], which chemically absorbs CO_2, is used as the electrolyte and the sensing element. It is worth mentioning that by changing the IL, the same platform architecture can detect other gases of interest sensitively and selectively. The chemical absorption of CO_2 in the IL causes compositional changes impacting the viscosity and ionic conductivity besides changes in chemical identities, thus ultimately having a direct, measurable response in the charge transfer resistance in the impedance spectrum and the peak current in the CV curve. Two different electrode configurations (NEC and FEC) were used to detect the changes in the impedance spectrum. NEC and FEC configurations showed similar sensitivity with LOD of 0.82 and 0.53 ppm, respectively. However, FEC showed better reproducibility compared to the NEC configuration. In the future, the structure of the microfluidic platform can be modified to perform gas-liquid contacting within the chip to detect gases in situ.

ORCID

Saudagar Dongare https://orcid.org/0000-0001-6782-0028
Burcu Gurkan https://orcid.org/0000-0003-4886-3350
Sagnik Basuray https://orcid.org/0000-0001-9767-9096

References

1. G. F. Fine, L. M. Cavanagh, A. Afonja, and R. Binions, "Metal oxide semiconductor gas sensors in environmental monitoring." *Sensors*, **10**, 5469 (2010).
2. M. Leidinger, T. Sauerwald, T. Conrad, W. Reimringer, G. Ventura, and A. Schütze, "Selective detection of hazardous indoor VOCs using metal oxide gas sensors." *Procedia Engineering*, **87**, 1449 (2014).
3. J. E. Ellis and A. Star, "Carbon nanotube based gas sensors toward breath analysis." *ChemPlusChem*, **81**, 1248 (2016).

4. G. Lee, O. Hossain, S. Jamalzadegan, Y. Liu, H. Wang, A. C. Saville, T. Shymanovich, R. Paul, D. Rotenberg, and A. E. Whitfield, "Abaxial leaf surface-mounted multimodal wearable sensor for continuous plant physiology monitoring." *Sci. Adv.*, **9**, eade2232 (2023).

5. S. Lakkis, R. Younes, Y. Alayli, and M. Sawan, "Review of recent trends in gas sensing technologies and their miniaturization potential." *Sensor Rev.*, **34**, 24 (2014).

6. W. Jing, W. Zhao, S. Liu, L. Li, C.-T. Tsai, X. Fan, W. Wu, J. Li, X. Yang, and G. Sui, "Microfluidic device for efficient airborne bacteria capture and enrichment." *Anal. Chem.*, **85**, 5255 (2013).

7. S. Kaaliveetil, J. Yang, S. Alssaidy, Z. Li, Y.-H. Cheng, N. H. Menon, C. Chande, and S. Basuray, "Microfluidic gas sensors: detection principle and applications." *Micromachines*, **13**, 1716 (2022).

8. F. Hossein-Babaei and V. Ghafarinia, "Gas analysis by monitoring molecular diffusion in a microfluidic channel." *Anal. Chem.*, **82**, 8349 (2010).

9. M. Ghazi, S. Janfaza, H. Tahmooressi, N. Tasnim, and M. Hoorfar, "Selective detection of VOCs using microfluidic gas sensor with embedded cylindrical microfeatures coated with graphene oxide." *J. Hazard. Mater.*, **424**, 127566 (2022).

10. F. Hossein-Babaei and A. Hooshyar, "Zare, The selective flow of volatile organic compounds in conductive polymer-coated microchannels." *Sci. Rep.*, **7**, 42299 (2017).

11. M. Ghazi, S. Janfaza, H. Tahmooressi, A. Ravishankara, E. Earl, N. Tasnim, and M. Hoorfar, "Enhanced selectivity of microfluidic gas sensors by modifying microchannel geometry and surface chemistry with graphene quantum dots." *Sensors Actuators B*, **342**, 130050 (2021).

12. M. Paknahad, J. S. Bachhal, A. Ahmadi, and M. Hoorfar, "Characterization of channel coating and dimensions of microfluidic-based gas detectors." *Sensors Actuators B*, **241**, 55 (2017).

13. B. D. Piorek, S. J. Lee, J. G. Santiago, M. Moskovits, S. Banerjee, and C. D. Meinhart, "Free-surface microfluidic control of surface-enhanced Raman spectroscopy for the optimized detection of airborne molecules." *Proc. Natl Acad. Sci.*, **104**, 18898 (2007).

14. B. D. Piorek, S. J. Lee, M. Moskovits, and C. D. Meinhart, "Free-surface microfluidics/surface-enhanced Raman spectroscopy for real-time trace vapor detection of explosives." *Anal. Chem.*, **84**, 9700 (2012).

15. K. Yang, S. Zong, Y. Zhang, Z. Qian, Y. Liu, K. Zhu, L. Li, N. Li, Z. Wang, and Y. Cui, "Array-assisted SERS microfluidic chips for highly sensitive and multiplex gas sensing." *ACS Appl. Mater. Interfaces*, **12**, 1395 (2019).

16. K. Yang, K. Zhu, Y. Wang, Z. Qian, Y. Zhang, Z. Yang, Z. Wang, L. Wu, S. Zong, and Y. Cui, "Ti3C2T x MXene-loaded 3D substrate toward on-chip multi-gas sensing with surface-enhanced raman spectroscopy (SERS) barcode readout." *ACS Nano*, **15**, 12996 (2021).

17. L. Xiong and R. G. Compton, "Amperometric gas detection: A review." *Int. J. Electrochem. Sci.*, **9**, 7152 (2014).

18. P. K. Sekhar, D. Graf, O. Ojelere, T. K. Saha, M. A. Riheen, and S. Mathur, "Electrochemical gas sensor integrated with vanadium monoxide nanowires for monitoring low concentrations of ammonia emission." *J. Electrochem. Soc.*, **167**, 027548 (2020).

19. H. Yuan, N. Li, W. Fan, H. Cai, and D. Zhao, "Metal-organic framework based gas sensors." *Adv. Sci.*, **9**, 2104374 (2022).

20. I. Raya, H. H. Kzar, Z. H. Mahmoud, A. Al Ayub Ahmed, A. Z. Ibatova, and E. Kianfar, "A review of gas sensors based on carbon nanomaterial." *Carbon Letters*, 1 (2021).

21. C. V. Raju, C. H. Cho, G. M. Rani, V. Manju, R. Umapathi, Y. S. Huh, and J. P. Park, "Emerging insights into the use of carbon-based nanomaterials for the electrochemical detection of heavy metal ions." *Coord. Chem. Rev.*, **476**, 214920 (2023).

22. R. Bhardwaj and A. Hazra, "MXene-based gas sensors." *J. Mater. Chem. C*, **9**, 15735 (2021).

23. R. Umapathi, C. V. Raju, S. M. Ghoreishian, G. M. Rani, K. Kumar, M.-H. Oh, J. P. Park, and Y. S. Huh, "Recent advances in the use of graphitic carbon nitride-based composites for the electrochemical detection of hazardous contaminants." *Coord. Chem. Rev.*, **470**, 214708 (2022).

24. E. W. Graef, R. D. Munje, and S. Prasad, "A robust electrochemical CO 2 sensor utilizing room temperature ionic liquids." *IEEE Trans. Nanotechnol.*, **16**, 826 (2017).

25. E. W. Graef, B. Jagannath, R. Munje, and S. Prasad, "Fluorinated anionic room temperature ionic liquid-based CO 2 electrochemical sensing." *IEEE Sens. J.*, **18**, 3517 (2018).

26. M. Ge, G. Hussain, D. B. Hibbert, D. S. Silvester, and C. Zhao, "Ionic liquid-based microchannels for highly sensitive and fast amperometric detection of toxic gases." *Electroanalysis*, **31**, 66 (2019).

27. G. Hussain, M. Ge, C. Zhao, and D. S. Silvester, "Fast responding hydrogen gas sensors using platinum nanoparticle modified microchannels and ionic liquids." *Anal. Chim. Acta*, **1072**, 35 (2019).

28. D. S. Silvester, "Recent advances in the use of ionic liquids for electrochemical sensing." *Analyst*, **136**, 4871 (2011).

29. A. Rehman and X. Zeng, "Methods and approaches of utilizing ionic liquids as gas sensing materials." *RSC Adv.*, **5**, 58371 (2015).

30. Y.-H. Cheng, R. Kargupta, D. Ghoshal, Z. Li, C. Chande, L. Feng, S. Chatterjee, N. Koratkar, R. K. Motkuri, and S. Basuray, "ESSENCE–A rapid, shear-enhanced, flow-through, capacitive electrochemical platform for rapid detection of biomolecules." *Biosens. Bioelectron.*, **182**, 113163 (2021).

31. Z. Li, Y.-H. Cheng, C. Chande, S. Chatterjee, and S. Basuray, "A highly sensitive, easy-and-rapidly-fabricable microfluidic electrochemical cell with an enhanced three-dimensional electric field." *Anal. Chim. Acta*, **1232**, 340488 (2022).

32. Y. H. Cheng, D. Barpaga, J. A. Soltis, V. Shutthanandan, R. Kargupta, K. S. Han, B. P. McGrail, R. K. Motkuri, S. Basuray, and S. Chatterjee, "Metal–organic framework-based microfluidic impedance sensor platform for ultrasensitive detection of perfluorooctanesulfonate." *ACS Appl. Mater. Interfaces*, **12**, 10503 (2020).

33. M. B. Shiflett and A. Yokozeki, "Chemical absorption of sulfur dioxide in room-temperature ionic liquids." *Ind. Eng. Chem. Res.*, **49**, 1370 (2010).

34. Z. Li, X. Zhang, H. Dong, X. Zhang, H. Gao, S. Zhang, J. Li, and C. Wang, "Efficient absorption of ammonia with hydroxyl-functionalized ionic liquids." *RSC Adv.*, **5**, 81362 (2015).

35. L. M. Galán Sánchez, G. W. Meindersma, and A. B. Haan, "Potential of silver-based room-temperature ionic liquids for ethylene/ethane separation." *Ind. Eng. Chem. Res.*, **48**, 10650 (2009).

36. A. Ortiz, L. Maria Galan, D. Gorri, A. B. de Haan, and I. Ortiz, "Reactive ionic liquid media for the separation of propylene/propane gaseous mixtures." *Ind. Eng. Chem. Res.*, **49**, 7227 (2010).

37. Y.-Y. Lee, K. Edgehouse, A. Klemm, H. Mao, E. Pentzer, and B. Gurkan, "Capsules of reactive ionic liquids for selective capture of carbon dioxide at low concentrations." *ACS Appl. Mater. Interfaces*, **12**, 19184 (2020).

38. S. Seo, M. A. DeSilva, and J. F. Brennecke, "Physical properties and CO2 reaction pathway of 1-ethyl-3-methylimidazolium ionic liquids with aprotic heterocyclic anions. The." *J. Phys. Chem. B*, **118**, 14870 (2014).

39. Y.-Y. Lee and B. Gurkan, "Graphene oxide reinforced facilitated transport membrane with poly (ionic liquid) and ionic liquid carriers for CO2/N2 separation." *J. Membr. Sci.*, **638**, 119652 (2021).

40. A. Shrivastava and V. B. Gupta, "Methods for the determination of limit of detection and limit of quantitation of the analytical methods." *Chron. Young Sci*, **2**, 21 (2011).

41. U. Dinish, F. C. Yaw, A. Agarwal, and M. Olivo, "Development of highly reproducible nanogap SERS substrates: comparative performance analysis and its application for glucose sensing." *Biosens. Bioelectron.*, **26**, 1987 (2011).